Atmospheric Research 328 (2026) 108415

Contents lists available at ScienceDirect

Atmospheric Research

journal homepage: www.elsevier.com/locate/atmosres

Decade-long variability of winter aerosols in East Asia and their associations with climatic factors

Yeomin Jeong [a], Na-Mi Lee [b], Wonbae Jeon [a,c], Jung-Woo Yoo [a], Maeng-Ki Kim [d], Suryun Ham [e], Cheol-Hee Kim [a,c,*]

[a] Institute of Environmental Studies, Pusan National University, Busan 46241, Republic of Korea
[b] Numerical Modeling Center, Korea Meteorological Administration, Daejeon 35208, Republic of Korea
[c] Department of Atmospheric Sciences, Pusan National University, Busan 46241, Republic of Korea
[d] Department of Atmospheric Science, Kongju National University, Gongju 32588, Republic of Korea
[e] Climate Services and Research Division, APEC Climate Center, Busan 48058, Republic of Korea

ARTICLE INFO

Keywords:
Aerosol optical depth
East Asia
Emissions
Western pacific oscillation
East Asian winter monsoon
Arctic Sea ice

ABSTRACT

East Asia has historically experienced high atmospheric aerosol concentrations, particularly during winter, when aerosol optical depth (AOD) reaches its peak level and exhibits significant variability. This study investigated the long-term variability of wintertime AOD over East Asia, including statistical associations with emission trends from the Emissions Database for Global Atmospheric Research (EDGAR), climate factors including the Western Pacific Oscillation (WPO), East Asian Jet Stream Index (EAJSI), Siberian High Index (SHI), and Arctic Sea Ice Index (ASI) in December–February from 2000 to 2022. An empirical orthogonal function (EOF) analysis revealed that although reductions in both NO_x and SO_2 emissions have significantly contributed to a long-term decrease in AOD, the pronounced intra-seasonal and interannual variability suggests additional influences from climate factors. The most prominent EOF mode of AOD variability was observed in February, along with strong associations with the SHI, EAWMI, and EAJSI. Climate indices related to the EAWMI exerted a stronger influence in late winter (February), partly due to intensified mid-latitude westerlies during the mature phase of the EAWMI. In contrast, the WPO primarily influenced early-winter AOD variability (December–January) by altering upper-level pressure patterns over the western Pacific, enhancing the EAJSI and modulating AOD distribution across the China–Korea region—a pattern that has become more evident in recent years. Furthermore, the rapid decline in Arctic Sea ice during early winter appeared to strengthen both the SHI and the EAJSI, leading to a decrease in AOD by late winter. These findings highlight the increasing importance of climate factors in influencing wintertime AOD over East Asia.

1. Introduction

Rapid economic growth and industrialization have resulted in East Asia having some of the highest aerosol concentrations in the world, resulting in severe air pollution problems (Feng et al., 2016; He et al., 2017; Pei et al., 2018). Estimates suggest that approximately 300,000 premature deaths occur annually in East Asia due to aerosol exposure (Kauffmann and Saffirio, 2020). In response to the worsening air pollution levels since the early 2010s, many East Asian countries have implemented stringent emission reduction policies (Zhang et al., 2016; Lee et al., 2018). While these regulations have led to a decline in aerosol concentrations, levels in East Asia remain higher than those in Europe and North America (Shin et al., 2023; Zheng et al., 2018), particularly during winter, when severe air pollution episodes occur more frequently (Ding and Liu, 2014; Gao et al., 2021; Cai et al., 2017).

High aerosol concentrations are influenced by both anthropogenic emissions and the meteorological conditions that regulate atmospheric circulation (Choi et al., 2023; Kim et al., 2023; Kim et al., 2018). While long-term trends in aerosol concentrations primarily reflect changes in emissions, short-term and seasonal variability is largely driven by interannual fluctuations in meteorological factors (Lang et al., 2017; Jeong et al., 2024). Xu et al. (2024) identified emission reductions as the main driver of air quality improvement across China, but also reported that unfavorable meteorological conditions in northeastern China offset

* Corresponding author at: Department of Atmospheric Sciences, Pusan National University, San 30, Jangjeon-Dong, Geumjeong-Gu, Busan 609-735, South Korea.
E-mail address: chkim2@pusan.ac.kr (C.-H. Kim).

https://doi.org/10.1016/j.atmosres.2025.108415
Received 20 April 2025; Received in revised form 26 July 2025; Accepted 6 August 2025
Available online 7 August 2025

these benefits, resulting in only minimal reductions in aerosol concentrations. Similarly, Zhao et al. (2018) found that an intensified Siberian High triggered strong northerly winds over the North China Plain, leading to reductions in aerosol levels comparable to those achieved by a 50 % emission cut. Jeong et al. (2024) further demonstrated that recent winter aerosol concentration variability in South Korea was largely attributed to changes in meteorological conditions, accounting for contributions of up to 17 %. Collectively, these findings highlight the significant role of atmospheric circulation in shaping air quality across East Asia and the potential for interannual climate variability to influence aerosol levels alongside emission control measures.

The East Asian Winter Monsoon (EAWM) transports cold and dry air from the northwest, shaping the region's cold and dry seasonal climate. Several studies have reported that the strength and position of the EAWM influence the interannual variability of aerosol concentrations in East Asia (Chen et al., 2019; Yin et al., 2017; Zou et al., 2017). Jeong and Park (2017) analyzed air pollution patterns using the East Asian Winter Monsoon Index (EAWMI) and found that aerosols are transported from north to south during strong EAWM phases, resulting in lower concentrations in northern China and elevated levels in southern regions. They also reported that fine particulate matter ($PM_{2.5}$) concentrations can vary by up to 25 % depending on the monsoon's strength. The East Asian Jet Stream (EAJS), which is modulated by the intensity of the EAWM, plays a critical role in transporting cold air from high latitudes. Lee et al. (2020) proposed that a weakened EAJS leads to increased aerosol concentrations in East Asia due to enhanced stagnation caused by slower westerly winds transporting air masses from high to mid-latitudes. Similarly, Zhang et al. (2022a, 2022b) found that a northward shift of the EAJS weakens the East Asian trough, increases atmospheric stability over eastern China, and creates favorable conditions for aerosol accumulation.

In addition to the EAWM and jet stream dynamics, climate factors such as Arctic Sea ice and Eurasian snow cover can influence mid-latitude atmospheric circulation (Kim et al., 2014), thereby affecting regional meteorological conditions and aerosol distributions (Yin et al., 2017). As Arctic warming accelerates under ongoing climate change, the "Warm Arctic, Cold Eurasia" (WACE) pattern has become more prominent, altering the position and strength of upper-level jet streams that are critical for modulating the spatial distribution and intensity of aerosol concentrations across China (Yin et al., 2019; Zhang et al., 2022a, 2022b). Kim et al. (2019) also reported that loss of sea ice in the Barents Sea can intensify the EAWM, leading to increased aerosol concentrations in South Korea due to stronger upper-level westerlies.

Previous studies in East Asia have provided valuable insights into the relationship between winter aerosol concentrations and the EAWM and Arctic Sea ice variability. However, other major climate indices that may affect aerosol variability—particularly the Western Pacific Oscillation (WPO), East Asian Jet Stream Index (EAJSI), Siberian High Index (SHI), and Arctic Sea ice Index (ASI)—have received comparatively less attention. Among these, the WPO, primarily driven by changes in sea surface temperature (SST) distributions, is of particular interest: it represents an upper-level pressure anomaly over the northwestern Pacific that typically emerges before the onset of the EAWM. Several studies have reported that the WPO plays a critical role in modulating the strength and position of the EAJS (Park and Ahn, 2016).

So far, broader-scale climate modes associated with SST—such as the El Niño–Southern Oscillation (ENSO) and the Pacific Decadal Oscillation (PDO)—have been extensively studied for their associations with winter haze events in eastern China (Wang et al., 2020; Zhao et al., 2016; Zhao et al., 2022). Unlike ENSO and PDO, the WPO is more regionally confined to the western North Pacific and exhibits stronger sub-seasonal variability. During its positive phase, the WPO reinforces the Siberian High, thereby enhancing the EAWM; in its negative phase, it weakens the monsoon and increases the likelihood of atmospheric stagnation (Takaya and Nakamura, 2013). These features suggest that the WPO may act as a distinct and dynamic modulator of aerosol variability, particularly through its influence on upper-level circulation and jet stream behavior. Despite its potentially important role, however, the WPO's impact on aerosol concentrations in East Asia remains largely unexamined.

Given the impact of ongoing climate change on winter conditions in East Asia, it is crucial to conduct such analyses using the most current data available. Our dataset included wintertime AOD data, which provide comprehensive spatial coverage across East Asia. We adopted an integrative approach by considering both emission trends and the interannual variability of multiple climate drivers—including the WPO, EAJSI, SHI, and ASI—to examine aerosol–climate interactions using long-term satellite-based AOD observations. This integrated framework enabled us to clarify the underlying mechanisms driving aerosol concentration variability and our findings provide a robust scientific basis for future air quality management strategies in East Asia.

The remainder of this paper is organized as follows. Section 2 details the data and methods used, including information on AOD, emissions, and relevant climate indices. Section 3.1 analyzes the long-term monthly variability of winter AOD across East Asia. Section 3.2 examines long-term trends in emissions associated with AOD. Section 3.3 identifies the dominant spatial modes of aerosol concentration variability using statistical decomposition and assesses their temporal evolution, and then explores the relationships between these modes and major climate indices, including the potential impact of recent ASI decline on aerosol variability. Finally, Section 4 summarizes the key findings and their broader implications.

2. Data and methodology

2.1. Study area

East Asia, including China, Korea, and Japan, is one of the most densely populated regions in the world and has some of the highest AOD levels globally. We selected four key regions to represent the major sources of anthropogenic air pollutant emissions in East Asia: the North China Plain (NCP), Sichuan Basin (SCB), Pearl River Delta (PRD), and Korea Region (KR), as shown in Fig. 1. These regions were selected based on the spatial distribution of emissions and their standard deviations (Supplementary Fig. 1). They are high-emission zones (Section 3.2) and correspond to the major loading centers of an empirical orthogonal function (EOF) analysis (Section 3.3).

The NCP includes major administrative regions such as Beijing, Tianjin, Hebei, Shandong, Henan, Shanxi, Jiangsu, and Anhui, and represents the most significant anthropogenic emission center in China. Emission levels in this region exhibit strong seasonal and interannual variability, primarily driven by industrial production, coal combustion for heating, and vehicular emissions. The SCB, which includes Sichuan

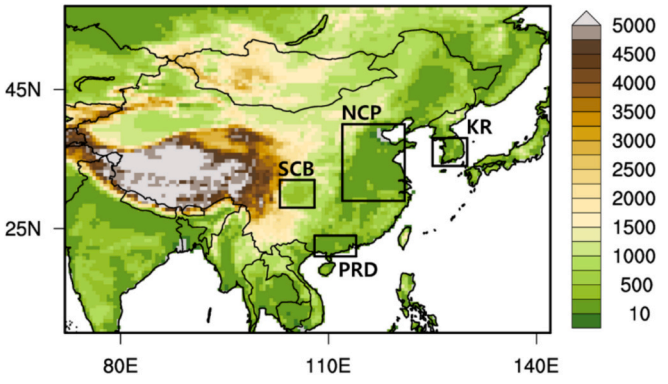

Fig. 1. Elevation (m) and sub-regions (black solid line) of the study area. The sub-regions are as follows: North China Plain (NCP), Sichuan Basin (SCB), Pearl River Delta (PRD), and Korea Region (KR).

Province and parts of Chongqing Municipality, is geographically enclosed by mountains, resulting in frequent atmospheric stagnation. Major urban centers such as Chengdu and Chongqing contribute to the region's relatively high regional emissions.

The PRD region includes major cities such as Guangzhou, Shenzhen, Foshan, and Dongguan. The region is a major economic, industrial, and port hub in southern China and exhibits considerable spatiotemporal variability in aerosol concentrations. Its coastal location exposes the region to strong maritime influences, which increase the variability in pollutant dispersion and accumulation. The KR region approximately corresponds to the Seoul metropolitan area and its surrounding regions. It is characterized by a high density of urban, industrial, and vehicular emission sources and serves as a key region for analysis of transboundary pollution in East Asia.

The elevated risk of high AOD levels in these selected regions has been corroborated by several previous studies (Leung et al., 2018; Jin et al., 2022; Xu et al., 2024). For analytical simplicity, simple rectangular domains were used to define the four sub-regions—NCP, SCB, PRD, and KR—which may not perfectly align with administrative boundaries. To support spatial visualization and analysis, publicly available geographic information system (GIS) data were used to delineate national boundaries, which were overlaid on the AOD distribution fields. Taiwan and offshore islands were excluded from the boundary depiction in accordance with the original GIS dataset settings.

2.2. Study period

The study period was determined based on data availability and extended from the winter of 2000 (when satellite observations became available) to the winter of 2022, the most recent season for which a comprehensive emission inventory is available. This timeframe encompassed 22 winter seasons (December, January, February), from December 2000 to February 2022; in this context, "winter 2001" refers to the period covering December 2000, January 2001, and February 2001, in accordance with the meteorological definition of winter.

To assess recent trends in comparison to the entire study period, we also selected a sub-period representing the past decade (winters of 2013–2022). This enabled us to isolate and identify the recent driving factors influencing changes in AOD patterns; the findings from the past decade have implications for air quality policies across the study region.

2.3. Methodology

The study methodology included a variety of statistical techniques. An EOF analysis was conducted using normalized, gridded monthly mean AOD data to ensure comparability across subdivided spatial and temporal scales. The normalization process removed the mean (spatial or temporal, as appropriate) and scaled the data to unit variance, enabling identification of the dominant variability patterns. The EOF analysis decomposed the AOD dataset into orthogonal modes that captured the largest sources of variance (Ma et al., 2021; Tian et al., 2023a, 2023b) through the calculation of eigenvectors and eigenvalues of the covariance matrix.

The resulting EOFs represent spatial patterns of variability, while the associated principal components (PCs) describe the temporal evolution of these patterns. The first EOF mode (EOF 1), which accounted for the largest fraction of total variance, was selected for our analysis because it reflects the predominant spatial pattern of AOD variability. The corresponding time series (PC1) was analyzed to examine the temporal evolution of this EOF 1 pattern and to track changes in the distribution of AOD over time.

To explore potential climate drivers, Pearson correlation coefficients (R) were calculated between PC1 and several climate indices: WPO, EAJSI, and SHI, considering both simultaneous and lagged correlations to capture the delayed atmospheric responses. Time series and spatial correlation analyses were also conducted between the ASI and major atmospheric circulation systems to assess how sea ice variability may influence East Asian winter circulation patterns, and in turn affect AOD levels.

Correlation analyses were conducted for both the full 22-winter period (2001−2022) and the recent 10-winter sub-period (2013−2022). Student's *t*-tests were used to assess whether the differences between the two periods were statistically significant. Although the sample size for the recent sub-period was relatively small ($n = 10$), this targeted analysis was critical to identify recent shifts in AOD patterns and their driving mechanisms. Statistical significance was evaluated using the critical t-values corresponding to the 99 %, 95 %, and 90 % confidence levels.

For visualization, spatial correlation maps were generated to identify regions where AOD variability exhibited strong associations with specific climate indices. Notably, the sign of PC1 was reversed in the correlation maps to enhance the interpretability of the spatial relationships.

2.4. Data

A suite of datasets was employed to examine the relationship between aerosol variability and climate factors over East Asia. A summary of the datasets used is provided below, with additional details listed in Table 1.

2.4.1. Aerosol data

Monthly mean AOD at 550 nm was obtained from the Moderate Resolution Imaging Spectroradiometer (MODIS) sensors onboard NASA's Terra and Aqua satellites, covering the period from 2000 to 2022. We used the latest Collection 6.1, which has demonstrated improved accuracy and a strong correlation with AERONET ground-based observations, particularly over Northeast China, which was the focal region of this study (Filonchyk et al., 2019). The MODIS AOD has been widely validated and is regarded as a reliable proxy for aerosol concentrations at regional to continental scales (Wei et al., 2019; Tian and Gao, 2019; Shaheen et al., 2020).

2.4.2. Emission data

To explore the relationships between AOD and anthropogenic emissions, we analyzed sulfur dioxide (SO_2) and nitrogen oxides (NO_x) data from the Emissions Database for Global Atmospheric Research (EDGAR), version 8.1. This dataset offers spatially detailed, monthly global emissions categorized by sector, including energy production, industry, transportation, and residential sources. Monthly total emissions were derived by aggregating emissions from these individual sectors.

2.4.3. Meteorological and climate data

Meteorological fields and climate indices were derived from the ERA5 reanalysis provided by the European Centre for Medium-Range Weather Forecasts (ECMWF). Monthly anomalies were computed relative to the 1981–2020 climatological mean. The key variables included sea level pressure (SLP), 500 hPa geopotential height (Z500), and 300 hPa zonal wind (U300), which characterize the large-scale wintertime circulation patterns over East Asia.

We also analyzed several climate indices: the SHI, EAWMI, and EAJSI (Jhun and Lee, 2004; Yang et al., 2002). We also included the WPO index due to its significant influence on upper-level circulation. The WPO reflects a meridional dipole in geopotential height over the North Pacific and is known to modulate the strength and position of the EAJS. It is generally in a positive phase when negative anomalies occur over the WPO1 region and positive anomalies occur over the WPO2 region, as shown in Fig. 2. Due to its association with SST, the WPO exhibits slow variability, potentially affecting AOD levels via jet stream modulation.

Table 1
Summary of the aerosol, emissions, atmospheric, and oceanic data used in this study.

Abbreviations	Data name	Source	Analysis period	Spatial resolution	Description
AOD	Aerosol optical depth	NASA	2000-2022 (Dec-Feb)	1°x1°	Dark Target and Deep Blue (550 nm)
NO_x	Nitrogen oxides	EDGAR	2000-2022 (Dec-Feb)	0.1°x0.1°	EDGAR version8.1 Global Air Pollutant Emissions
SO_2	Sulfur dioxide				
SLP	Sea level pressure	ECMWF	2000-2022 (Dec-Feb)	0.25°x0.25°	Climate values used to calculate anomalies are from 1981 to 2020
Z500	Geopotential height at 500 hPa				
U300/V300	U/V component of wind at 300 hPa				
Temp.	Temperature				Analysis of meridional cross sections from 1000 to 100 hPa.
U-wind w	U component of wind vertical velocity				
WPO	Western Pacific Oscillation index	NOAA PSL	2000-2022 (Dec-Feb)	-	Downloaded from NOAA PSL website
SIC	Sea ice concentration	Met Office Hadley Centre	2000-2022 (Nov-Feb)	1°x1°	Calculates Arctic Sea Ice Index (ASI) by normalizing area averaged SIC (Lee and Kim, 2021).

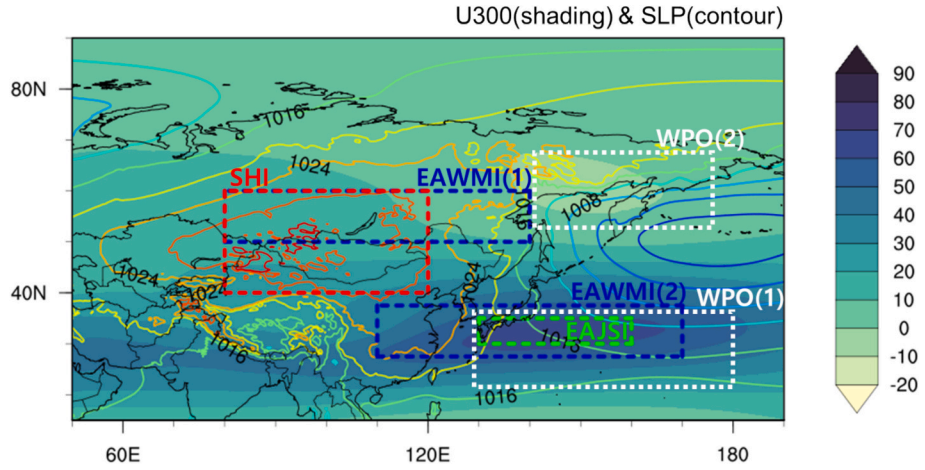

Fig. 2. Climatological U300 (shading, m s^{-1}) and SLP (contour line, hPa) during the boreal winter. The domains for calculating climate indices are indicated: SHI (red box), EAWMI (blue boxes, EAWMI1 − EAWMI2), EAJSI (green box), and WPO (white boxes). (For interpretation of the references to colour in this figure legend, the reader is referred to the web version of this article.)

2.4.4. Sea ice data

To assess the Arctic influence, we used sea ice concentration (SIC) data from the Hadley Centre Sea Ice and Sea Surface Temperature dataset (HadISST). The ASI was calculated by standardizing SIC values over regions dynamically linked to the EAWM (Lee and Kim, 2021). The ASI enabled us to investigate the potential impact of Arctic Sea ice decline on mid-latitude circulation patterns and its subsequent influence on wintertime AOD variability in East Asia.

3. Results

3.1. Spatial distribution and long-term trends of wintertime AOD in East Asia

Table 2 presents the statistical summary of wintertime AOD—mean, maximum, minimum, and standard deviation—across East Asia during the analysis period from 2001 to 2022. Fig. 3 illustrates both the spatial distributions of seasonal mean AOD and the interannual variation in each of the four representative regions: NCP, SCB, PRD, and KR. Over the entire region, a 57.1 % increase in mean AOD from December to February was observed, indicating a clear seasonal rise in aerosol loading during winter. This increase was systematic across all four subregions, with the most prominent rise occurring in the SCB, followed by the NCP, KR, and PRD.

Table 2
Monthly AOD mean, maximum, minimum, and standard deviation for East Asia and its sub-regions during the winter season (2000−2022).

		EA	NCP	SCB	PRD	KR
Dec.	**mean**	0.21	0.48	0.45	0.47	0.24
	min	0.18	0.35	0.32	0.29	0.18
	max	0.26	0.62	0.72	0.81	0.34
	stddev	0.02	0.08	0.09	0.14	0.04
Jan.	**mean**	0.27	0.62	0.48	0.55	0.30
	min	0.21	0.41	0.26	0.39	0.20
	max	0.32	0.88	0.68	0.78	0.42
	stddev	0.03	0.13	0.09	0.10	0.06
Feb.	**mean**	0.33	0.70	0.75	0.58	0.34
	min	0.23	0.43	0.50	0.37	0.20
	max	0.45	1.13	1.17	0.79	0.51
	stddev	0.05	0.18	0.20	0.12	0.07

The NCP consistently exhibited the highest mean AOD levels throughout the winter, especially in February, likely due to dense emission sources and unfavorable meteorological dispersion conditions

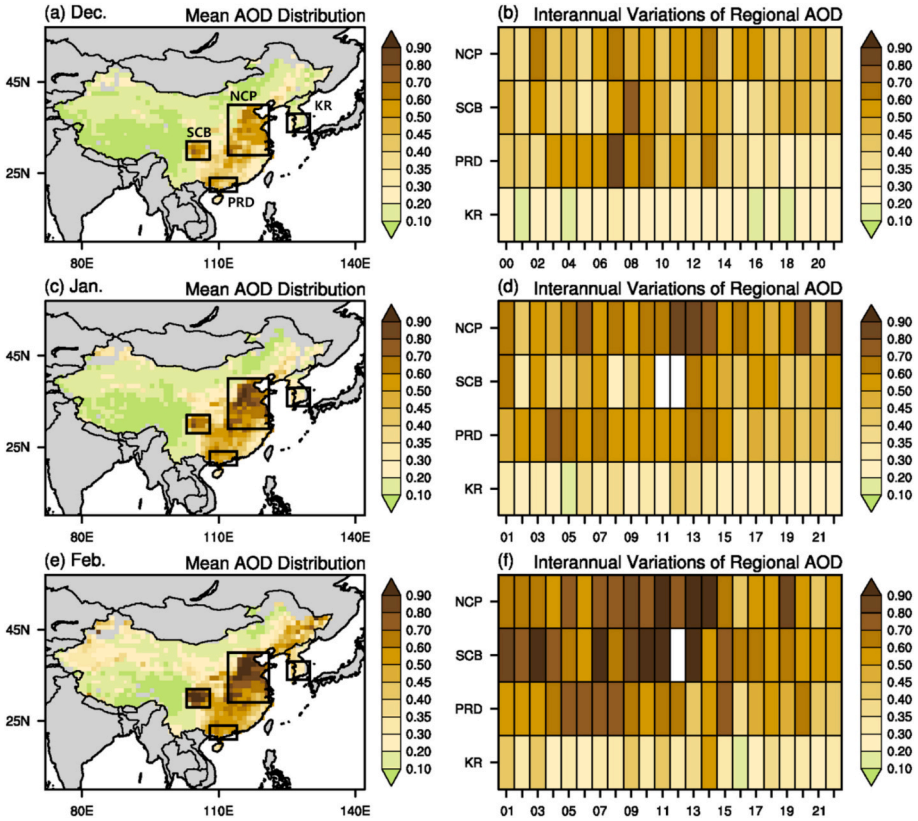

Fig. 3. Spatial distribution of the mean AOD in (a) December, (c) January, and (e) February over the entire period (winters of 2000–2022), and interannual AOD changes in (b) December, (d) January, and (f) February for the four sub-regions. Satellite observations with more than 40 % of data missing are blanked.

(Zhang et al., 2018a, 2018b). Similarly, the SCB showed elevated AOD levels, peaking in February, which can be attributed to the combined effects of basin-induced atmospheric stagnation and increased emissions from winter heating (Liao et al., 2018). In contrast, the PRD, located at lower latitudes, displayed relatively stable AOD with minor seasonal changes. The KR region generally maintained the lowest AOD among the four regions, with less variability over the winter months.

In terms of variability, the standard deviation of AOD also increased from December to February, particularly in the NCP and SCB. The SCB saw a 122.2 % increase in standard deviation, while the NCP followed closely, indicating heightened interannual fluctuations during late winter in these inland regions. These findings suggest that both the magnitude and variability of AOD tend to increase as winter progresses.

Fig. 4 and Supplementary Table 1 compare long-term trends in AOD for two distinct periods: the full 22-year period (2001–2022) and the most recent decade (2013–2022). Across most regions, moderate decreasing trends were observed over the full period, with annual rates ranging from −0.16 % to −0.26 %. However, these trends became significantly stronger during the past decade, especially in February, when the rates of decline accelerated to between −0.51 % and −1.10 % per year. In some regions, such as the NCP and SCB, the decline in February AOD exceeded 4 % per year during the past decade.

Notably, the NCP showed a contrasting pattern across the two periods. While January AOD had increased slightly (0.29 % per year) over the entire period, a sharp reversal was observed during the past decade, with January and February AOD decreasing at rates of −1.89 % and −4.70 % per year, respectively—the latter being the steepest decline among all cases examined. A similar shift occurred in the SCB, where a relatively mild decline during the full period intensified to a steep reduction in recent years. The PRD exhibited its strongest decreasing trend in December, while the KR also showed roughly threefold stronger declines in the past decade compared to the earlier period.

The observed long-term and recent trends in spatial and temporal patterns point to significant improvements in wintertime air quality across East Asia, reflecting the combined effects of seasonal emissions, meteorological conditions, and long-term policy impacts. Overall, the observed spatial and temporal patterns reflect the combined effects of seasonal emissions, meteorological conditions, and long-term policy impacts.

3.2. *Long-term changes in emissions of air pollutants associated with AOD*

To explore associations between AOD trends and changes in emissions, we analyzed variations in SO_2 and NO_x emissions, which are the primary precursors of particulate matter affecting AOD levels. Our EDGAR emissions data (see section 2.4) revealed that the annual variations of SO_2 and NO_x emissions during the three months of December, January, and February were strongly correlated, with average inter-month R of 0.98–0.99 (for SO_2) and 0.89–0.90 (for NO_x). Therefore, we used the three-month average emissions (December–February) normalized to an annual time series, instead of separating the data by individual months. As shown in Fig. 5a and b, wintertime (December–February) three-month mean emissions of NO_x and SO_2 were concentrated in NCP, SCB, PRD, and KR. Particularly high concentrations were observed along the eastern coastal areas of NCP, reflecting the region's dense population and intensive industrial activity.

Specifically, NO_x emissions (mean ± standard deviation, unit: Gton/per unit area) were highest (8.1 ± 0.2) in the NCP and were comparable to the PRD (8.1 ± 0.1), followed by the KR (4.8 ± 0.1) and SCB (3.4 ± 0.1). For SO_2, the highest emissions occurred in the NCP (11.4 ± 0.3), followed by the PRD (10.0 ± 0.4), SCB (4.5 ± 0.1), and KR (4.1 ± 0.1) (Figs. 5c). Of particular interest is the PRD region, which exhibited higher emissions than the SCB, although the AOD was much higher in the SCB (see Fig. 3 and Fig. 4). This discrepancy could be attributed to

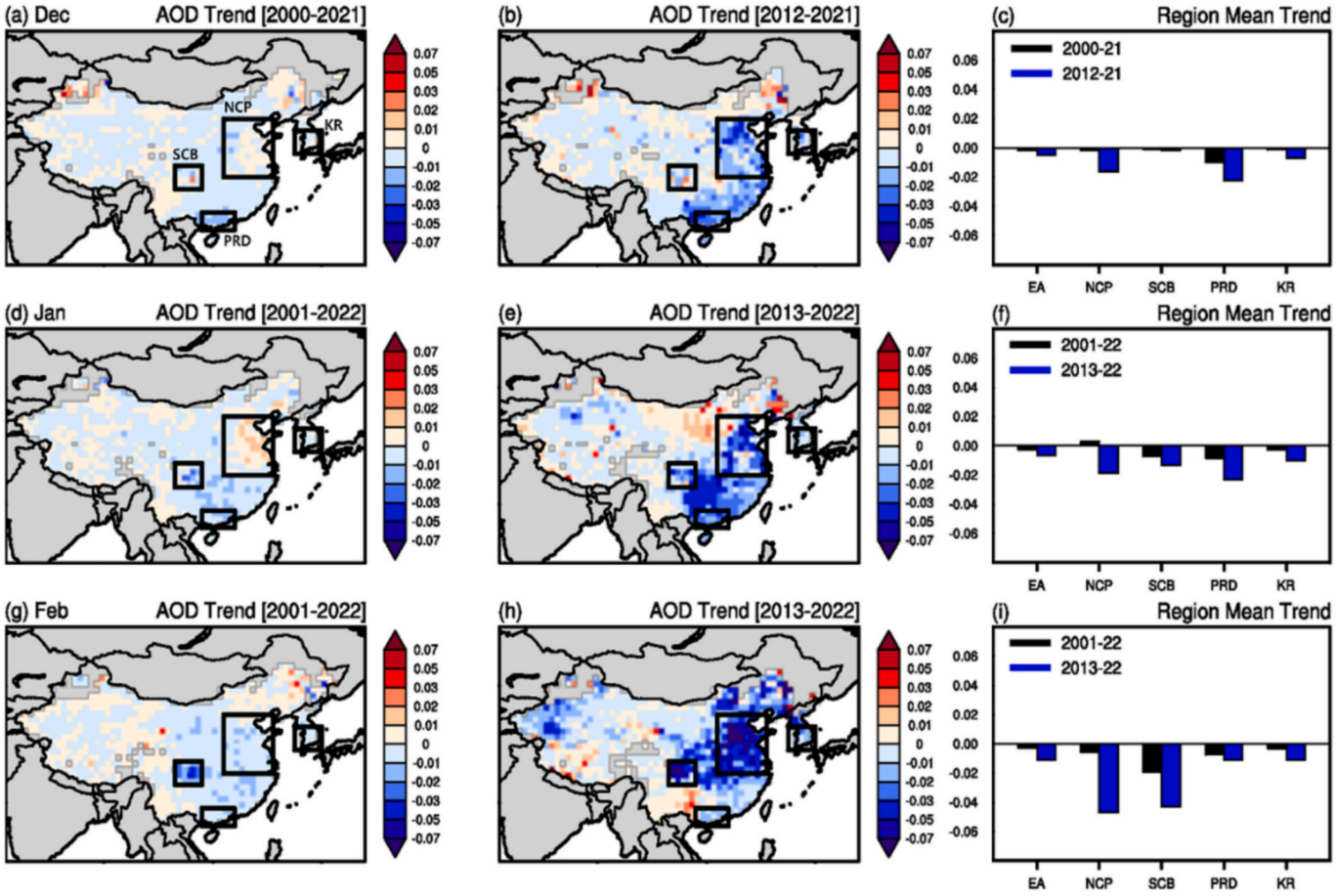

Fig. 4. Spatial distribution of the AOD trend in December (top), January (middle), and February (bottom). Left panel: (a), (d), and (g) show the trends for the entire period (winters of 2000–2022). Middle panel: (b), (e), and (h) show the trends for the past decade (winters of 2013–2022). Right panel: (c), (f), and (i) show the regional mean trends in East Asia and each of the four sub-regions for the entire period (black bars) and the past decade (blue bars). (For interpretation of the references to colour in this figure legend, the reader is referred to the web version of this article.)

the basin-shaped topography of the SCB, which limited atmospheric dispersion and facilitated the accumulation of air pollutants.

Emission trends over the past decade showed consistent decreases in both NO_x and SO_2 across most regions (Fig. 5d). The most pronounced reductions were observed in the NCP, suggesting the effectiveness of China's air pollution control policies (Zhang et al., 2019; Zheng et al., 2018). The PRD had minimal reductions in NO_x emissions; the emission control measures adopted in PRD have been described in more detail by Peng et al. (2011) and Wang et al. (2021). Fig. 5e and f present the winter emission trends for NO_x and SO2, respectively, normalized to their 2013 values. Most mainland China regions have experienced a steady decline in SO2 and NOx emissions since 2013. For NO_x, the largest decreases were observed in the NCP and SCB, with a similar rate of decrease for SO2 in the major Chinese regions (i.e., the NCP, SCB, and PRD). The corresponding trends in the KR region differed from those in mainland China. A sharp reduction was observed in both NO_x and SO2 around 2018, marking the most pronounced decline in the past decade. This substantial reduction was likely associated with the implementation of stronger air quality management policies, including the "Air Pollution Prevention and Control Action Plan" implemented in China in 2013, as well as the "Special Act on Fine Dust Reduction" that was enacted in South Korea (Malley et al., 2023; Oak et al., 2025).

These reductions contributed to the primary decrease in AOD levels. The AOD decline recorded here is consistent with previous ground-based and satellite observations (Zhang et al., 2019; Zheng et al., 2018). While the emissions trends in these sub-regions generally showed linear annual changes, except for around 2019, the monthly variability in AOD exhibited secondary characteristics, such as nonlinear trends and discrepancies with emission patterns (Fig. 3). Therefore, we examined additional factors affecting AOD variability, including climate influences.

3.3. AOD in association with climate factors

The association between AOD and the EAWM has been well established in previous studies. Specifically, lower AOD levels are attributed to the ventilation effects of a strengthened northwesterly monsoon, which effectively disperses air pollutants (Kim et al., 2019; Zou et al., 2017). As in previous studies, we conducted a more comprehensive analysis using statistical approaches, including simultaneous and lagged correlations between various atmospheric systems. We identified the dominant patterns of monthly AOD variability and explored their simultaneous and lagged relationships with the climate indices primarily associated with the EAWM.

3.3.1. Dominant mode analysis of winter AOD

Fig. 6 presents the spatial patterns and temporal evolution of the first principal component (PC1) of wintertime AOD variability for the EOF 1 mode over three months. In December, strong positive signals were centered over the PRD, followed by the NCP, explaining 31.4 % of the total variance. In January, a prominent positive pattern was observed over the NCP, accounting for 32.6 %. By February, the positive anomalies extended across the NCP, SCB, and KR, covering a broader spatial extent with an explanatory power of 47.2 %. These findings indicate that

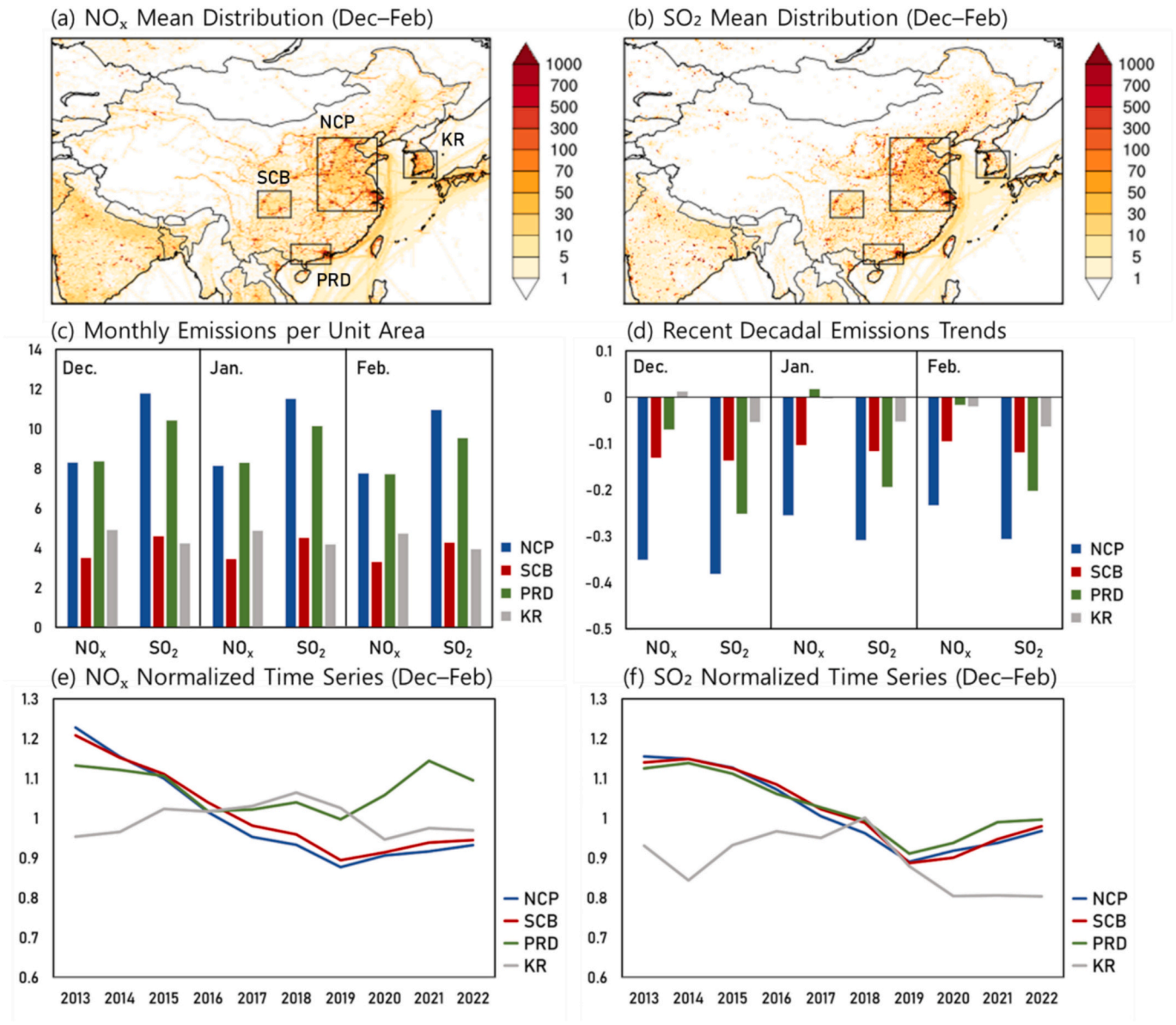

Fig. 5. Spatiotemporal distribution of EDGARv8.1 emissions for NO_x (left panel) and SO_2 (right panel) (Ton) during the winter season (2000–2022): (a) and (b) spatial distributions; (c) monthly emissions per unit area (1° × 1°) for each sub-region (Gt); (d) changes over the past decade in each of the sub-regions (Gt); (e) and (f) time series of the annual changes of emissions normalized to 2013.

coherent AOD variability is most extensive in February in East Asia. Consequently, the dominant spatial pattern of wintertime AOD in the region is centered over northern and southern China, with a broader and stronger expansion in February, closely linked to interannual variability primarily driven by the NCP.

The time series of PC1 revealed positive anomalies from the mid-2000s to the early 2010s, and negative anomalies from 2013/14 to 2022. These findings indicate that the recent decline in wintertime AOD levels was effectively captured by the dominant mode. Table 3 lists the regional and monthly R between annual AOD variations and PC1, which further supports these findings. In the PRD, the strongest correlation ($R = 0.91$) between AOD variation and PC1 occurred in December. In the NCP, the strongest associations were observed in January and February ($R = 0.97$ and 0.93, respectively), and a robust relationship was also observed in December ($R = 0.72$). In the PRD, the weaker correlation in January and February may be linked to regional emission patterns, but a detailed analysis of this was beyond the scope of this investigation. The KR region consistently exhibited significant positive correlations throughout all three months, with the strongest values observed in February. These EOF analysis results effectively captured the monthly spatiotemporal patterns of the East Asian winter season and highlighted the interannual variability across sub-regions.

3.3.2. *AOD dominant modes versus East Asian winter climate factors*

To clarify the climate drivers behind the recent changes in AOD in East Asia, we compared the interannual variability of the AOD-EOF 1 mode with climate fluctuations associated with the EAWM. We calculated R for the relationships between EOF PC1 and four climate indices: SHI, EAWMI, EAJSI, and WPO.

Table 4 lists R for the relationship between the AOD PC1 time series and EAWMI in wintertime (December, January, and February): values on the main diagonal represent R without a time lag, and values in parentheses represent correlations for the past decade. For most climate indices, more significant changes were observed in the past decade for both simultaneous (non-lagged) and one-month lagged correlations of climate indices such as SHI, EAWMI, EAJSI, and WPO. Among the four

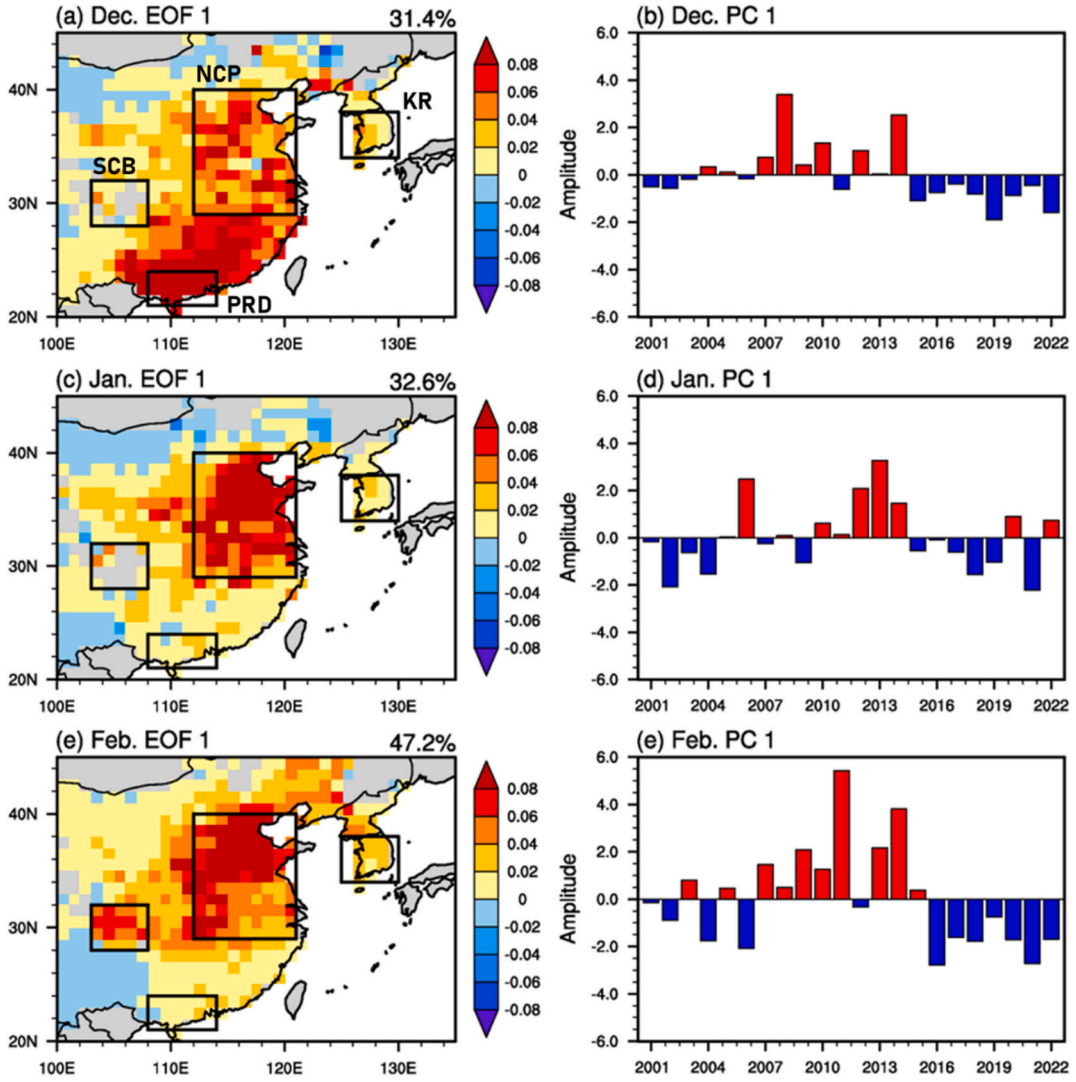

Fig. 6. (a) Spatial patterns and (b) time series of the first EOF mode of monthly AOD in December during the entire period (winters of 2000–2022). January is represented in (c–d) and February in (e–f). The explanatory power of the first mode is 31.4 %, 32.6 %, and 47.2 % for December, January, and February, respectively.

Table 3
Correlation coefficients between the time series of the first mode of monthly AOD EOF and the interannual change in sub-regions. Significance is indicated by ***, **, and *, which correspond to 99 %, 95 %, and 90 % confidence levels, respectively.

		NCP	SCB	PRD	KR
EOF PC1	Dec.	0.72***	0.31	0.91***	0.69***
	Jan.	0.97***	0.49**	0.18	0.47**
	Feb.	0.93***	0.59***	0.23	0.78***

climate indices, the non-lagged EAJSI in February had an R of −0.75, the maximum observed in our study, followed by WPO with an R of −0.74 in December, and SHI for December–January with a lagged R of −0.64 in the past decade. These results suggest that the driving mechanism in East Asia is the WPO in early winter, and the EAJSI and SHI in mid- and late-winter. It was also notable that a statistically significant simultaneous correlation was observed in February: both the EAWMI and the EAJSI were negatively correlated with PC1, with R of −0.51 ($p < 0.05$) and −0.60 ($p < 0.01$), respectively. These results suggest that enhanced upper-tropospheric westerlies over East Asia increase the surface wind speeds, thereby promoting the dispersion of pollutants through both ventilation processes and enhanced mechanical mixing in the boundary layer.

The physical mechanisms behind this relationship in February can be further explained by referring to previous research. The strengthening of the jet stream is known to enhance horizontal winds in the upper troposphere (approximately 200–300 hPa), thereby promoting horizontal advection and vertical mixing. In turn, intensified jet activity reinforces upper-level divergence, which induces a weak upward motion near the surface. These processes contribute to an increase in the mixing layer height, alleviate near-surface atmospheric stagnation, and further facilitate the dispersion and removal of surface-level pollutants. Despite reduced anthropogenic emissions (see Fig. 5), the pronounced variability in AOD in February can be influenced by the large-scale upper-level atmospheric circulation. Previous EOF analyses have revealed that the explanatory power of EOF PC1 is approximately 60 % higher in February compared to December and January.

In the early-winter period, the simultaneous correlation of WPO-PC1 in December was relatively weak over the entire period ($R = -0.22$), but it strengthened considerably in the past decade, reaching a statistically significant negative correlation ($R = -0.74$, $p < 0.10$). The lagged-R value for the December WPO vs. January PC1 relationship exhibited a significant negative correlation PC1 ($R = -0.57$, $p < 0.01$) during the entire period, and this relationship persisted during the past decade ($R = -0.56$, $p < 0.10$) (see Table 4). These findings suggest that when the

Table 4
Monthly correlation coefficients of the AOD PC1 time series with East Asian winter monsoon climate indices. Values in brackets denote the data from the past decade, and lagged correlations are displayed in italicized form. Significance is indicated by ***, **, and *, corresponding to the 99 %, 95 %, and 90 % confidence levels, respectively.

AOD	SHI					
	Dec. (Recent decade)		Jan. (Recent decade)		Feb. (Recent decade)	
Dec.	−0.30	(−0.36)				
Jan.	*0.01*	(*−0.22*)	0.01	(−0.49)		
Feb.			*0.10*	(*−0.64***)	−0.21	(0.15)

AOD	EAWMI					
	Dec. (Recent decade)		Jan. (Recent decade)		Feb. (Recent decade)	
Dec.	−0.05	(0.05)				
Jan.	*0.29*	(*−0.09*)	0.09	(−0.18)		
Feb.			*0.19*	(*−0.49*)	−0.51**	(−0.42)

AOD	EAJSI					
	Dec. (Recent decade)		Jan. (Recent decade)		Feb. (Recent decade)	
Dec.	0.11	(0.46)				
Jan.	*0.39*	(*0.09*)	0.15	(0.10)		
Feb.			*0.43***	(*0.05*)	−0.60***	(−0.75**)

AOD	WPO					
	Dec. (Recent decade)		Jan. (Recent decade)		Feb. (Recent decade)	
Dec.	−0.22	(−0.74**)				
Jan.	*−0.57****	(*−0.56**)	−0.20	(−0.49)		
Feb.			*−0.23*	(*−0.26*)	−0.37*	(0.41)

December WPO is in a positive phase, the AOD in East Asia tends to decrease in the following January. Therefore, the WPO is the driving mechanism with the most persistent impact on early-winter AOD variabilities in East Asia. In contrast, in February, the simultaneous correlation of WPO and AOD variability remained weak throughout the study period, and a negative correlation was observed in the past decade ($R = -0.37$, $p < 0.10$) in East Asia.

Based on these results, we further examined the driving mechanisms of early-winter AOD variability associated with the WPO and late-winter variability related to the SHI and EAJSI. Initially, we examined the correlation between AOD PC1 and the 500 hPa geopotential height (Z500) as well as the zonal wind component at 300 hPa (U300) during December to explore the WPO mechanism in early winter. Fig. 7 presents the spatial distributions of R for the relationships between Z500 vs. AOD-PC1 and U300 vs. AOD-PC1 in December. As shown in Fig. 7a, Z500 vs. AOD-PC1 revealed a distinct dipole structure: negative anomalies (in the northwestern Pacific) and positive anomalies (in the southwestern Pacific), which was indicative of the positive WPO phase. From an atmospheric dynamics perspective, this structure with a positive WPO phase enhances cyclonic circulation over the northwestern Pacific and anticyclonic circulation over the southwestern Pacific, thereby strengthening westerly flows across northeast Asia, including China, Korea, and southern Japan. Strengthened westerlies enhance the EAJS, promoting ventilation effects that contribute to reduced AOD levels. The relationship between U300 and AOD-PC1 (Fig. 7b) suggests that the upper-level zonal wind component intensifies the EAJS, supporting the hypothesis that changes in atmospheric circulation—and associated ventilation—linked to WPO phases influence AOD variability across East Asia.

For the late-winter period, we focused on February, examining the influence of two or more climate variables associated with the SHI and EAJSI. Fig. 8 presents the annual changes in PC1 along with SLP, Z500, and U300 in February over the entire period (Figs. 8a–c). This was compared to the recent decadal period in January (Figs. 8d–f), revealing significant simultaneous and lagged correlations. In the figures, dots indicate regions with statistically significant correlations at the 90 %

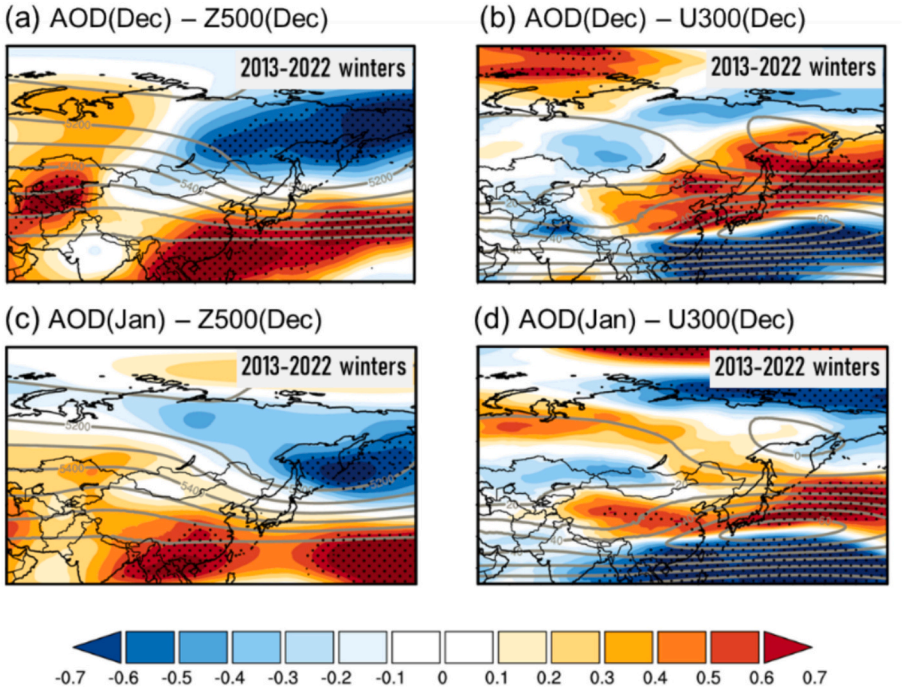

Fig. 7. Spatial distribution of the correlation coefficients between AOD PC1 in December and (a) Z500 (m) and (b) U300 (m s^{-1}) during the past decade (2012/13–2021/22 winters). Panels (c) and (d) present the corresponding fields for AOD PC1 in January. The gray solid line represents the 40-year (1981–2020) climatology. Dots indicate regions that were statistically significant at the 90 % confidence level.

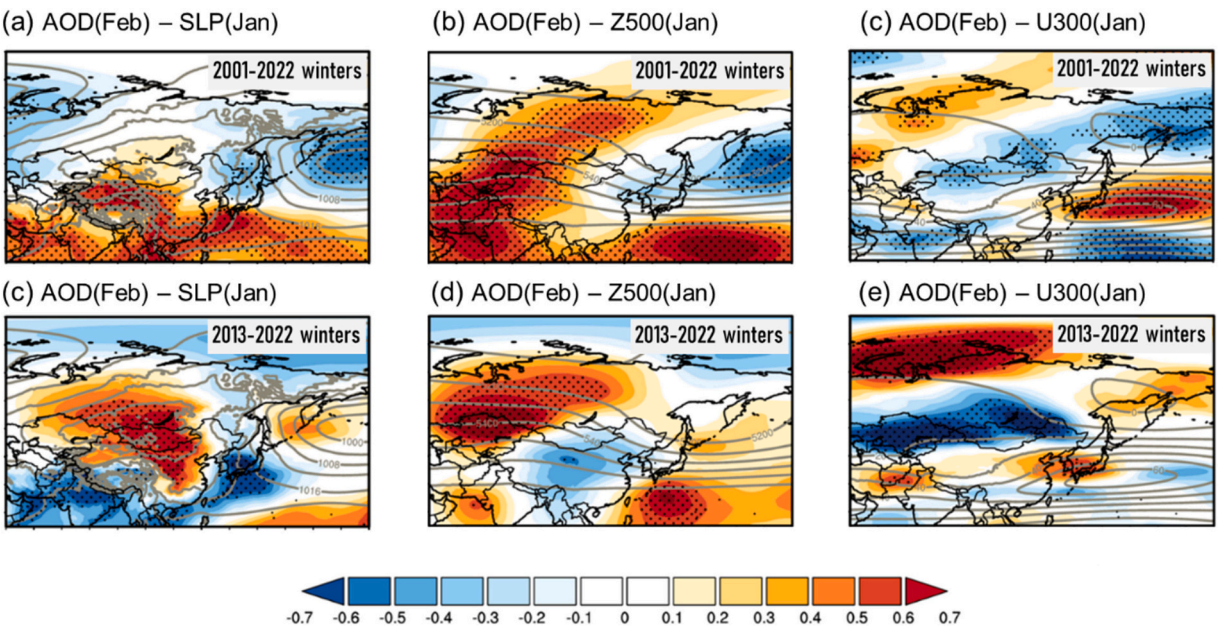

Fig. 8. Spatial distribution of the correlation coefficients between AOD PC1 in February and (a) SLP (hPa), (b) Z500 (m), and (c) U300 (m s^{-1}) during the entire period (winters of 2000/01–2021/22). Panels (d)–(f) show the same fields but for January during the past decade (winters of 2012/13–2021/22). The gray solid lines represent the 40-year climatology (1981–2020) and dots indicate regions significant at the 90 % confidence level.

confidence level. As shown in Fig. 8, the distribution of the correlations between January SLP and February PC1 over the past decade revealed a notable strengthening and expansion of the Siberian High (Fig. 8d) in comparison with the conditions in January over the entire analysis period (Fig. 8a). The associated Z500 pattern (Fig. 8e) in the past decade facilitated the southward intrusion of Arctic cold air into East Asia, leading to enhanced zonal wind fields and a subsequent reduction in AOD during February. The emergence of these atmospheric features exclusively in the past decade implies that recent climate shifts may be influencing wintertime AOD variability; further investigation will be needed to fully elucidate the mechanisms underlying these observed changes. A widespread positive Z500 anomaly (500 hPa high-pressure) over northwestern Eurasia was also observed in January (Fig. 8b) and February (Fig. 8d). This anomaly induced northwesterly winds and an intensified EAJS over the East China-Korea-Japan region (Fig. 8c), which continued to strengthen over the past decade (Fig. 8e). While the strengthening of the Siberian High enhances near-surface stability at its core, the periphery of the high-pressure system is characterized by

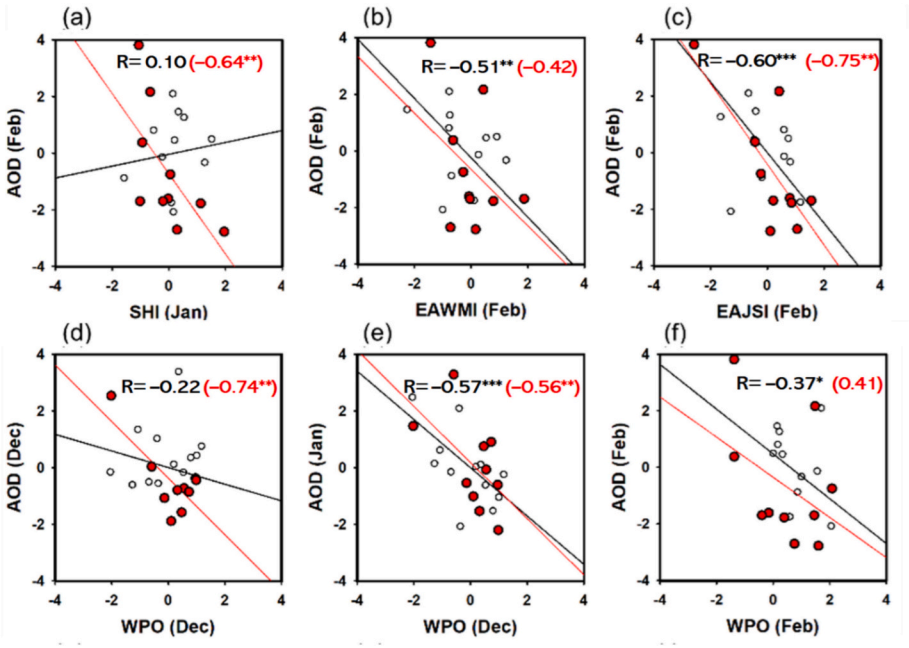

Fig. 9. Selected scatterplots showing the correlation coefficient (R) between AOD PC1 and various climate indices, with R values significant at the >90 % confidence level. Significance is indicated by ***, **, and *, corresponding to the 99 %, 95 %, and 90 % confidence levels, respectively, and values of R in brackets (shown in red) refer to data from the past decade. In each scatterplot, black circles and regression lines represent the entire period (winters from 2000 to 2022), while red circles and regression lines represent the past decade (winters from 2013 to 2022). (For interpretation of the references to colour in this figure legend, the reader is referred to the web version of this article.)

divergent outflows, leading to secondary circulations of surface flows from the high-pressure system toward adjacent lower-pressure regions. Given that the major East Asian sub-regions (e.g., eastern China, the Korean Peninsula, and Japan) are located near the southern or southeastern areas of the Siberian High, the intensified high pressure tends to promote surface ventilation. As a result of this mechanism, significant lagged negative correlations between February PC1 and SHI values ($r = -0.64$, $p < 0.05$) were found exclusively in the past decade (Table 4). These findings suggest a recent intensification of the roles of the SHI and EAJSI in relation to late-winter AOD in East Asia, contributing to the observed downward trend in February AOD levels. However, we did not observe such persistent circulation patterns in early winter (i.e., December).

Fig. 9 presents the selected scatterplots illustrating the correlations that are significant at the >90 % confidence level. As shown in the figure, the strongest non-lagged correlation was observed between the EAJSI and AOD PC1 in February, when both the AOD levels and the explanatory power of EOF1 reached their peak during the late-winter period (i.e., February in Table 4). A significant negative correlation was also found between the December WPO and AOD levels throughout the entire study period. These results suggest that the influence of climate factors on AOD has become more pronounced and regionally specific in recent years (see the red circles in Fig. 9), indicating a clear association between WPO and AOD variability, particularly during the early-winter season.

The WPO is primarily driven by changes in SST distributions, with a relatively small monthly variability. This small variation explains the lagged influence between the December WPO spatial structure and January AOD variability. Notably, January represents the peak stage period of the EAWM, during which the influence of the western Pacific on East Asian atmospheric circulation remains diminished. This resulted in no simultaneous correlation between WPO and PC1 in January (Table 4), while more significant associations were observed in the December WPO-January AOD relationship with R of −0.56 to −0.57. Therefore, the influence of the WPO on AOD variability was more prominent during the transitional phases of the EAWM, particularly in December and February, than the simultaneous early-winter response in East Asia. However, when focusing only on the recent decade (winters of 2012/13–2021/22), the R between WPO and AOD reaches as high as −0.74, indicating a substantially increased influence of the WPO on recent early-winter AOD variability in East Asia. This result implies that the WPO has played a particularly prominent role in modulating early-winter AOD levels in recent years, highlighting the need for continued attention to the WPO's influence in future analyses.

Our findings indicate that the dominant AOD mode over East Asia is influenced by multiple large-scale atmospheric factors, and that these relationships have become more pronounced over the past decade, particularly in association with early-winter WPO circulation. In addition, winter and spring meteorological conditions in East Asia frequently facilitate the transboundary transport of air pollutants (Lee et al., 2022; Kim et al., 2021; Jo and Kim, 2013). Considering these regional characteristics, and given that anthropogenic emissions in East Asia peak in December (see Fig. 5), our results further highlight the potential for linking early-winter emission reduction policies with climate influences—especially those associated with the WPO.

3.3.3. *Recent strengthening of Arctic variability and its linkage to late winter climate in East Asia*

As discussed in the previous section, the East Asian atmospheric circulation in January modulated the dominant AOD mode in February (SHI, $R = -0.64$, $p < 0.05$). We conducted further analysis to explore how early-winter (December) SIC changes affect mid-winter (January) EAWM dynamics. Our goal was to identify how alterations in monsoon structure may contribute to subsequent variations in AOD levels in East Asia during February.

Fig. 10 presents the distribution of the standard deviation of sea ice extent in December in the Barents Sea, a region closely related to EAWM variability (shaded areas in Fig. 10a), and the temporal (annual) variations of the December ASI over the past 22 years (2001–2022). Over this period, the Barents Sea ice cover has experienced a significant decline, particularly in the past decade, where most years have seen a reduction exceeding 0.5 standard deviations. The highlighted areas (hatched areas) in Fig. 10a indicate areas with significant variability in the January SHI, which exhibited a strong lagged correlation with the February AOD PC1 time series. The annual changes in the December ASI shown in Fig. 10b were calculated from the SIC for the region within the black solid line.

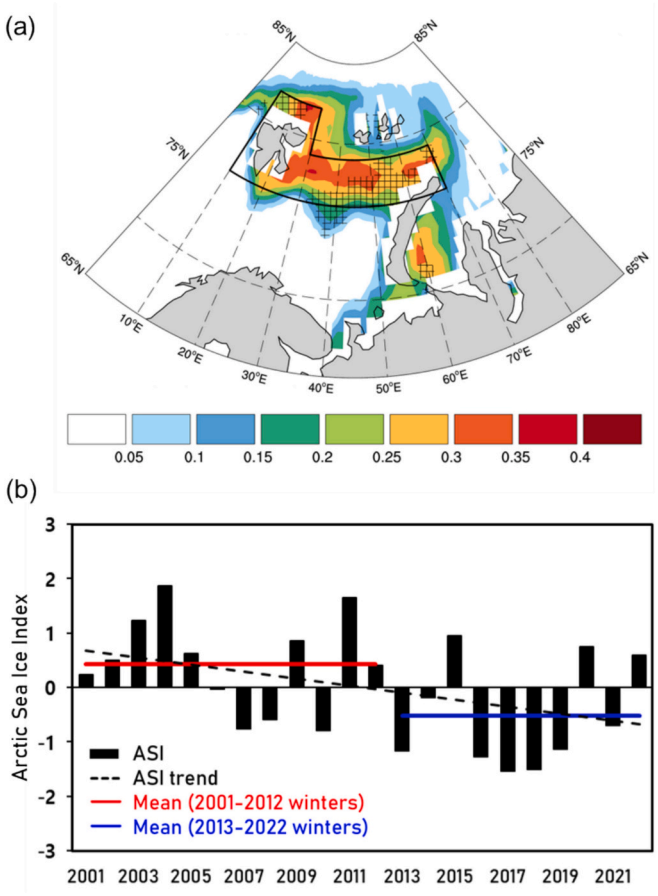

Fig. 10. (a) Spatial distribution of the standard deviation of SIC in December. Hatched areas indicate regions where the correlation with SHI was significant at the 80 % confidence level. The black outline denotes the area used to calculate the ASI. (b) Time series of the ASI, calculated by normalizing the area-averaged SIC over the Barents Sea (black box in panel (a)). The black dashed line indicates the linear trend, and the red and blue lines represent the mean values for the winters of 2001–2012 and 2013–2022, respectively. (For interpretation of the references to colour in this figure legend, the reader is referred to the web version of this article.)

To assess the impact of ASI variability on the EAWMI through the broader atmospheric dynamics during the winter months, we calculated the R for the relationship between the ASI and EAWMI for the three months (Table 5). As shown in Table 5, the SHI in February exhibited a significant lagged correlation with January ASI ($R = -0.43$, $p < 0.05$) and a non-lagged correlation in February ASI ($R = -0.62$, $p < 0.01$). This pattern implies that the heat flux released into the Arctic atmosphere due to decreasing sea ice weakens the polar vortex in the upper atmosphere over the Arctic, allowing cold air to move southward into East Asia, and strengthening the Siberian High, which is a cold continental high-pressure system. These findings align well with the results of previous studies that have linked polar variability to EAWM dynamics (Zou

Table 5
Monthly correlation coefficients between East Asian winter monsoon climate indices and the ASI. Values in brackets denote data from the past decade, and lagged correlations are displayed in italicized form. Significance is indicated by ***, **, and *, corresponding to the 99 %, 95 %, and 90 % confidence levels, respectively.

SHI	ASI							
	Nov. (Recent decade)		Dec. (Recent decade)		Jan. (Recent decade)		Feb. (Recent decade)	
Dec.	*0.33*	*(−0.04)*	0.08	(−0.04)				
Jan.	*−0.29*	*(−0.54)*	*−0.14*	*(−0.64**)*	−0.10	(−0.55)		
Feb.	*−0.32*	*(−0.28)*	*−0.30*	*(−0.19)*	*−0.40**	*(−0.07)*	−0.60***	(−0.49)

et al., 2017; Kim et al., 2019; Lee and Kim, 2021).

In January, the SHI had a statistically significant lagged correlation with December ASI ($R = -0.64$, $p < 0.05$), but this was only observed during the past decade. Similarly, the January SHI exhibited a significant lagged correlation with the February AOD ($R = -0.64$, $p < 0.05$), although this was again only limited to the past decade. These findings suggest that the rapid decline in early winter ASI (December) may have triggered a strengthening of the EAWM, subsequently contributing to the decrease in February AOD levels.

Fig. 11 presents a spatial correlation between January atmospheric conditions and December ASI over the past decade. Our analysis revealed that reduced sea ice led to the strengthening of the Siberian High (Fig. 11a), with a spatial distribution very similar to the pressure patterns associated with AOD variability in February (Fig. 8d). The distribution of the Z500 anomalies related to sea ice changes (Fig. 11b) indicates the development of a high-pressure system near the Barents–Kara Sea in the northern part of Eurasia, along with a corresponding low-pressure system that extended into Mongolia, northern China, and Korea. This configuration facilitated the southward movement of Arctic cold air into East Asia, inducing similar patterns linked to February AOD variability during the past decade (Fig. 8e). The reduction in sea ice also significantly intensified upper-level zonal winds over East Asia (Fig. 11c). These findings suggest that changes in ASI influence regional atmospheric circulation and AOD variability.

To further investigate the recent changes in the relationship between ASI variability and the EAWM, we examined differences in atmospheric structures between the past decade (winters of 2013–2022) and the earlier period (winters of 2001–2012). As shown in Fig. 11, a significant association between early-winter (December) sea ice loss and EAWM dynamics became evident, primarily in the past decade.

Fig. 12 presents the composite atmospheric fields from two analysis periods: the past decade (2013–2022) and the earlier period (2001−2012), which included negative winter ASI values as indicated in Fig. 10b. The negative ASI values during the earlier period were associated with high-pressure anomalies in the Barents Sea and low-pressure anomalies in the Chukchi and Bering Seas (Fig. 12a). However, in the past decade, high-pressure anomalies were observed across all Arctic Ocean regions, including the Barents Sea (Fig. 12b), presumably due to the weakening of the polar vortex driven by accelerated ASI decline (Kim et al., 2014).

In Fig. 10a, the region within the black box represents the area of greatest AOD variability in East Asia, as identified by the EOF analysis. We observed a consistent westerly anomaly in upper-level winds during both periods of sea ice decline. However, in the past decade, a more pronounced trough developed south of the Barents–Kara Sea, facilitating the influx of cold Arctic air toward East Asia.

Fig. 12 presents the meridionally averaged vertical composites of temperature anomalies and U-wind anomalies over the black box region for January (Figs. 12c–e) and February (Figs. 12f–h). When comparing periods of sea ice decline, the composites from the earlier period (Fig. 12c) exhibited a different atmospheric structure compared to the past decade (Fig. 12d). In the past decade (Fig. 12d), a dominant westerly wind anomaly extended from the upper to the lower atmosphere, accompanied by a negative temperature anomaly from the lower atmosphere to the surface over East Asia (20–40°N). These differences reveal that during periods of sea ice decline in the past decade, westerly winds (representing the EAJS) became more dominant in the upper troposphere, at around 200–300 hPa, while pronounced cold anomalies developed in the lower atmosphere, as shown in Fig. 12e. These cold air characteristics are likely the key factors explaining the statistically significant lagged relationship observed between the SHI and ASI.

The presence of vertical structures in February indicated a weakening of the upper-level jet stream and reduced temperature gradients compared to January (Figs. 12f–h). Nevertheless, strong upper-level westerly wind anomalies and persistent cold anomalies in the lower atmosphere over East Asia were still evident in February during the past decade (Fig. 12h).

A strengthened EAJS increases vertical wind shear, enhancing energy and momentum exchange between atmospheric layers. This intensification promotes convergence and divergence patterns in the lower troposphere, triggering vertical motion, particularly upward movement near the jet core. As a result, low-level stagnation is disrupted, planetary boundary layer height increases, and aerosol dispersion is facilitated. However, precipitation associated with this upward motion was not substantial in the main analysis regions due to low humidity conditions.

During the past decade, the decline in early-winter (December) ASI induced changes in East Asia's winter atmospheric structure, which was

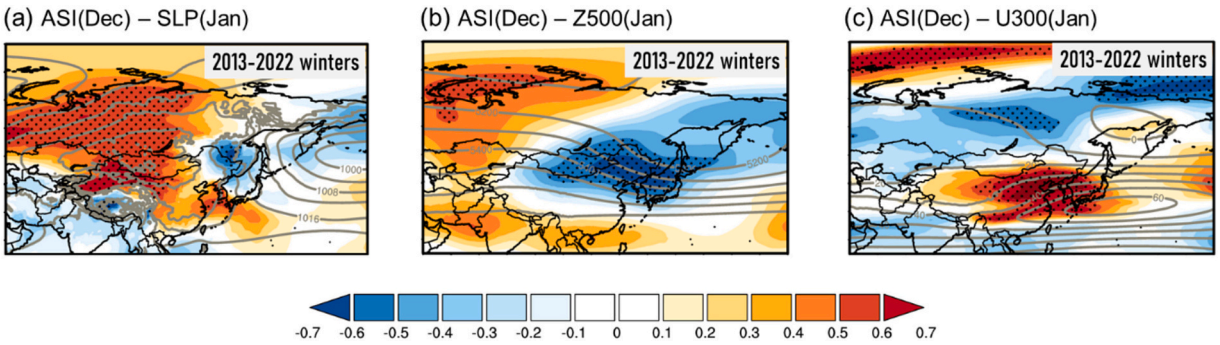

Fig. 11. Spatial distribution of the correlation coefficients between ASI in December and the atmospheric circulation for (a) SLP (hPa), (b) Z500 (m), and (c) U300 (m s^{-1}) in January during the past decade (2013–2022). The gray solid line represents the 40-year (1981–2020) climatology. Dots indicate significance at the 90 % confidence level.

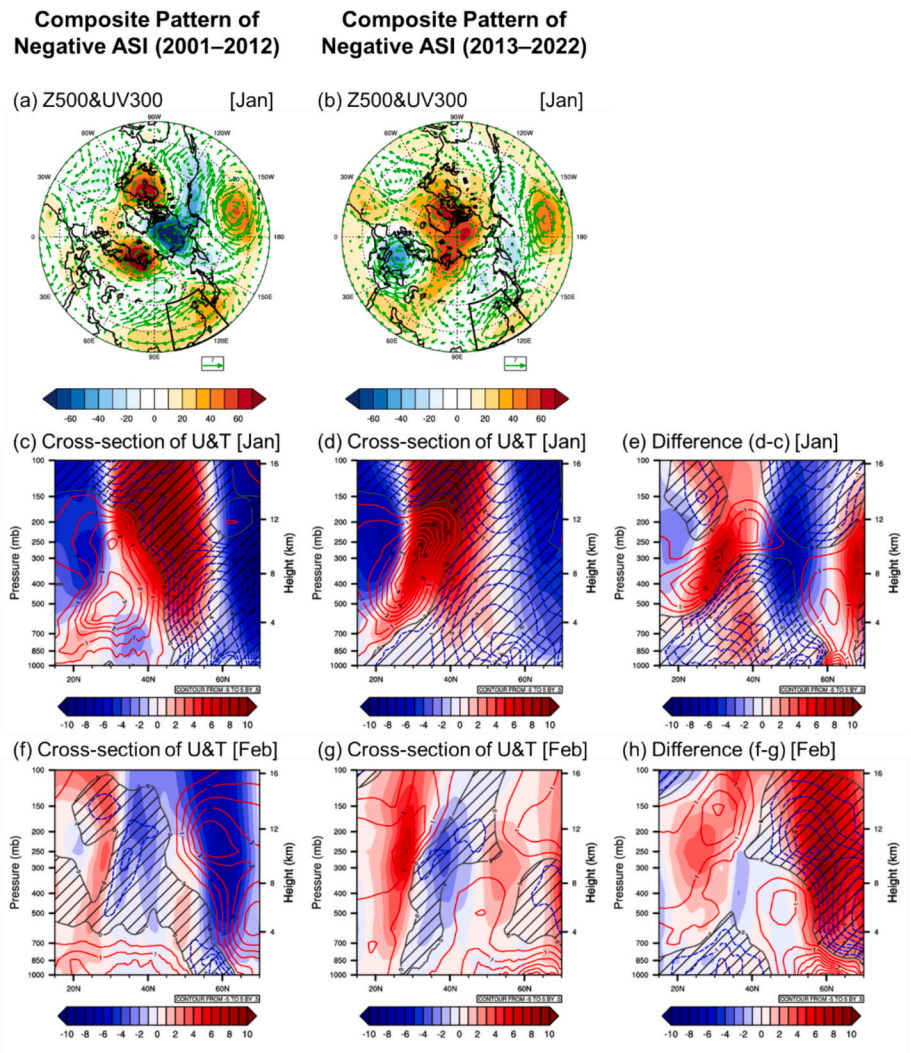

Fig. 12. Composite maps of Z500 anomalies (shading, m) and 300 hPa (U, V) wind vector anomalies associated with negative ASI events in January, for (a) 2001–2012 and (b) 2013–2022. Panels (c) and (d) present the meridionally averaged composite cross sections of temperature anomalies (contour) and U-wind anomalies (shading) over the black box region corresponding to (a) and (b), respectively. Panel (e) shows the difference between (d) and (c); panels (f)–(h) present the same analyses as (c)–(e), but for February data.

marked by intensified upper-level jet streams and enhanced lower-level cooling. Therefore, these structural changes may explain the observed lagged relationship between the SHI and ASI, and contribute to the continuation of atmospheric anomalies into January and February.

The statistical analysis revealed a significant negative correlation between February AOD and the EAJSI, a relationship that strengthened during the past decade. Vertical cross-sections of vertical velocity (w) (Supplementary Fig. 2) revealed more widespread upward motion during 2013–2022 compared to 2001–2012, which coincided with enhanced jet activity (Fig. 12). Furthermore, AOD levels across the major sub-regions decreased by an average of 18.4 % (ranging from 8 % to 32 %). Together, these results suggest that the strengthened winter jet stream likely plays a key role in modulating AOD variability through enhanced vertical mixing and dispersion processes.

4. Conclusion and discussion

We conducted a comprehensive assessment of the long-term variability of winter AOD in East Asia during 2001–2022, using satellite-derived AOD data. By examining the relationships between emission trends and large-scale climate drivers, we were able to identify the dominant mechanisms influencing regional AOD, and by extension, wintertime air quality.

We observed a general increase in wintertime AOD from December to February, with the highest concentrations and variability observed over the NCP and SCB. Since the early 2010s, however, the marked decline in AOD, especially in February, suggests substantial improvements in wintertime air quality across major pollution hotspots. Emission data revealed significant reductions in NO_x and SO_2 emissions across East Asia over the past decade, reflecting the effects of stringent air pollution control policies. These reductions were likely key contributors to the observed decline in wintertime AOD. Nevertheless, the large intra-seasonal and interannual variability in AOD contrasted with the relatively steady and linear decline in emissions, highlighting the importance of climate influences.

The timing of climate influences also exhibits clear seasonal variation. Monsoon-related indices such as the EAWMI, EAJSI, and SHI exert a stronger influence during the late-winter period (February), while the WPO predominantly affects AOD variability in early winter (December–January). Notably, the relationship between the WPO and early-winter AOD has become increasingly pronounced in recent years. This appears to be linked to a mechanism by which the WPO alters upper-level pressure patterns over the northwestern and southwestern Pacific, thereby enhancing the EAJS and modulating AOD distribution

across the China–Korea region.

The rapid decline in Arctic Sea ice during the early-winter period (December) over the past decade appears to have strengthened the upper-level westerlies in January. These circulation anomalies persisted into February, potentially shaping the large-scale meteorological conditions that contributed to the observed AOD decline. These findings suggest that the influence of Arctic variability on East Asian AOD levels could extend into late winter through the sustained anomalies in large-scale atmospheric circulation.

This study yielded important new insights, but it had some limitations. Our analyses were based primarily on monthly-scale statistical correlations, which may not capture finer-scale processes such as daily or intra-seasonal dynamics. Furthermore, the reliance on observational data restricted our ability to quantitatively disentangle the relative contributions of emissions versus climate drivers. More research will be needed to integrate higher-resolution temporal analyses and modeling approaches to more precisely quantify the interactions between emissions, climate variability, and AOD dynamics.

In conclusion, we demonstrated that recent improvements in East Asian wintertime air quality are driven not only by emission reductions but also by evolving climate influences, including mid-latitude atmospheric circulation and Arctic variability. These findings highlight the need to adopt integrated air quality management strategies that consider both anthropogenic and climate-related factors.

Funding

This research was supported by the Basic Science Research Program through the National Research Foundation of Korea (NRF), funded by the Ministry of Education (RS-2020-NR049592, RS-2023-00247459) and the National Research Foundation of Korea (NRF) grant funded by the Korea Government (MSIT) (RS-2023-NR076349).

Ethical approval

Not applicable.

Consent to participate

Not applicable.

Consent for publication

Not applicable.

CRediT author statement

Yeomin Jeong: Conceptualization, Methodology, Software, Data curation, Formal analysis, Investigation, Resources, Validation, Visualization, Writing – original draft, Writing – review & editing.

Na-Mi Lee: Data curation, Formal analysis, Investigation, Validation.

Wonbae Jeon: Funding acquisition, Writing – review & editing.

Jung-Woo Yoo: Data curation, Investigation, Validation.

Maeng-Ki Kim: Writing – review & editing.

Suryun Ham: Writing – review & editing.

Cheol-Hee Kim: Supervision, Conceptualization, Funding acquisition, Writing – review & editing.

CRediT authorship contribution statement

Yeomin Jeong: Writing – review & editing, Writing – original draft, Visualization, Validation, Resources, Methodology, Investigation, Formal analysis, Data curation, Conceptualization. **Na-Mi Lee:** Validation, Investigation, Formal analysis, Data curation. **Wonbae Jeon:** Writing – review & editing, Funding acquisition. **Jung-Woo Yoo:** Validation, Investigation, Data curation. **Maeng-Ki Kim:** Writing – review & editing. **Suryun Ham:** Writing – review & editing. **Cheol-Hee Kim:** Writing – review & editing, Supervision, Methodology, Investigation, Conceptualization.

Declaration of competing interest

The authors declare that they have no known competing financial interests or personal relationships that could have appeared to influence the work reported in this paper.

The author is an Editorial Board Member/Editor-in-Chief/Associate Editor/Guest Editor for this journal and was not involved in the editorial review or the decision to publish this article.

The authors declare the following financial interests/personal relationships which may be considered as potential competing interests:

Appendix A. Supplementary data

Supplementary data to this article can be found online at https://doi.org/10.1016/j.atmosres.2025.108415.

Data availability

Data will be made available on request.

References

Cai, W., Li, K., Liao, H., Wang, H., Wu, L., 2017. Weather conditions conducive to Beijing severe haze more frequent under climate change. Nat. Clim. Chang. 7, 257–262.

Chen, Y., Zhao, C., Ming, Y., 2019. Potential impacts of Arctic warming on Northern Hemisphere mid-latitude aerosol optical depth. Clim. Dyn. 53, 1637–1651. https://doi.org/10.1007/s00382-019-04706-3.

Choi, D., Lee, H.-J., Chang, L.-S., Jo, H.-Y., Jo, Y.-J., Park, S.-Y., Yang, G.-H., Kim, C.-H., 2023. Distinct meteorological mode associated with high-PM2.5 episodes in Seoul, South Korea. J. Appl. Meteorol. Climatol. 62, 853–862. https://doi.org/10.1175/JAMC-D-23-0016.1.

Ding, Y.H., Liu, Y.J., 2014. Analysis of long-term variations of fog and haze in China in recent 50 years and their relations with atmospheric humidity. Sci. China Earth Sci. 57 (1), 36–46.

Feng, S., Gao, D., Liao, F., Zhou, F., Wang, X., 2016. The health effects of ambient PM2.5 and potential mechanisms. Ecotoxicol. Environ. Saf. 128, 67–74. https://doi.org/10.1016/j.ecoenv.2016.01.030.

Filonchyk, M., Yan, H., Zhang, Z., Yang, S., Li, W., Li, Y., 2019. Combined use of satellite and surface observations to study aerosol optical depth in different regions of China. Sci. Rep. 9, 6174. https://doi.org/10.1038/s41598-019-42466-6.

Gao, Y., Zhang, M., Wu, C., 2021. Analysis of aerosol distribution variations over China for the period 2045–2050 under different representative concentration pathway scenarios. Atmosph. Ocean. Sci. Lett. 14 (2), 100027. https://doi.org/10.1016/j.aosl.2020.100027.

He, J., Gong, S., Yu, Y., Yu, L., Wu, L., Mao, H., Li, R., 2017. Air pollution characteristics and their relation to meteorological conditions during 2014–2015 in major Chinese cities. Environ. Pollut. 223, 484–496. https://doi.org/10.1016/j.envpol.2017.01.050.

Jeong, J.I., Park, R.J., 2017. Winter monsoon variability and its impact on aerosol concentrations in East Asia. Environ. Pollut. 221, 285–292. https://doi.org/10.1016/j.envpol.2016.11.075.

Jeong, J.I., Park, R.J., Song, C.-K., Yeh, S.-W., Woo, J.-H., 2024. Quantitative analysis of winter PM2.5 reduction in South Korea, 2019/20 to 2021/22: Contributions of meteorology and emissions. Sci. Total Environ. 907, 168179. https://doi.org/10.1016/j.scitotenv.2023.168179.

Jhun, J.-G., Lee, E.-J., 2004. A New East Asian Winter Monsoon Index and Associated Characteristics of the Winter Monsoon. J. Clim. 17 (5), 711–726. https://doi.org/10.1175/1520-0442(2004)017<0711:ANEAWM>2.0.CO;2.

Jin, Y., Ma, Y., Zhang, M., Liu, Y., Lu, X., Liu, B., Jin, S., Shen, A., Zhang, J., Fan, Q., 2022. Aerosol characteristics during the COVID-19 lockdown in China: Optical properties, vertical distribution, and potential source. Remote Sens. 14 (14), 3336. https://doi.org/10.3390/rs14143336.

Jo, H.-Y., Kim, C.-H., 2013. Identification of long-range transported haze phenomena and their meteorological features over Northeast Asia. J. Appl. Meteorol. Climatol. 52, 1318. https://doi.org/10.1175/JAMC-D-11-0235.1.

Kauffmann, C., Saffirio, C., 2020. Study of International Regulatory Co-operation (IRC) arrangements for air quality: the cases of the Convention on Long-Range Transboundary Air Pollution, the Canada-United States Air Quality Agreement, and co-operation in North East Asia. https://doi.org/10.1787/24140996.

Kim, B.-M., Son, S.-W., Min, S.-K., Jeong, J.-H., Kim, S.-J., Zhang, X., Shim, T., Yoon, J.-H., 2014. Weakening of the stratospheric polar vortex by Arctic Sea-ice loss. Nat. Commun. 5, 4646. https://doi.org/10.1038/ncomms5646.

Kim, C.-H., Lee, H.-J., Kang, J.-E., Jo, H.-Y., Park, S.-Y., Jo, Y.-J., Lee, J.-J., Yang, G.-H., Park, T., Lee, T., 2018. Meteorological overview and signatures of long-range

transport processes during the MAPS-Seoul 2015 campaign. Aerosol Air Qual. Res. 18 (9), 2173–2184. https://doi.org/10.4209/aaqr.2017.10.0398.
Kim, J.-H., Kim, M.-K., Ho, C.-H., Park, R.J., Kim, M.J., Lim, J., Kim, S.-J., Song, C.-K., 2019. Possible link between Arctic Sea ice and January PM10 concentrations in South Korea. Atmosphere 10 (10), 619. https://doi.org/10.3390/atmos10100619.
Kim, C.-H., Meng, F., Kajino, M., Lim, J., Tang, W., Lee, J.-J., Kiriyama, Y., Woo, J.-H., Sato, K., Kitada, T., Minoura, H., Kim, J., Lee, K.-B., Roh, S., Jo, H.-Y., Jo, Y.-J., 2021. Comparative Numerical Study of $PM_{2.5}$ in exit-and-entrance areas associated with transboundary transport over China, Japan, and Korea. Atmosphere 12, 469. https://doi.org/10.3390/atmos12040469.
Kim, C.-H., Jo, H.-Y., Jo, Y.-J., Lee, H.-J., Kim, J.-M., Lee, N.-M., Jeong, S.-Y., Baek, S.-H., Park, M.-J., Chang, L.-S., Lee, J.-J., Song, C.-K., 2023. Synoptic meteorological conditions and contributing factors to air quality during the SIJAQ campaign. Atmos. Environ. 309, 119939. https://doi.org/10.1016/j.atmosenv.2023.119939.
Lang, J., Zhang, Y., Zhou, Y., Cheng, S., Chen, D., Guo, X., Chen, S., Li, X., Xing, X., Wang, H., 2017. Trends of PM2.5 and chemical composition in Beijing, 2000-2015. Aerosol Air Qual. Res. 17, 412–425. https://doi.org/10.4209/aaqr.2016.07.0307.
Lee, N.-M., Kim, C.-H., 2021. Long-term Variations of Aerosol Optical Depth and their Associations with climate Change over East Asia. J. Korean Soc. Atmosph. Environ. 37 (6), 956–971. https://doi.org/10.5572/KOSAE.2021.37.6.956.
Lee, H.-J., Jeong, Y.-M., Kim, S.-T., Lee, W.-S., 2018. Atmospheric circulation patterns associated with particulate matter over South Korea and their future projection. J. Climate Change Res. 9 (4), 423–433. https://doi.org/10.15531/KSCCR.2018.9.4.423.
Lee, S., Lee, M.-I., Song, C.-K., Kim, K.-M., da Silva, A.M., 2020. Interannual variation of the East Asia Jet Stream and its impact on the horizontal distribution of aerosol in boreal spring. Atmos. Environ. 223. https://doi.org/10.1016/j.atmosenv.2020.117296.
Lee, H.-J., Jo, Y.-J., Kim, S., Kim, D., Kim, J.-M., Choi, D., Jo, H.-Y., Bak, J., Park, S.-Y., Jeon, W., Kim, C.-H., 2022. Transboundary aerosol transport process and its impact on aerosol- radiation-cloud feedbacks in springtime over Northeast Asia. Sci. Rep. 12, 4870. https://doi.org/10.1038/s41598-022-08854-1.
Leung, D.M., Tai, A.P.K., Mickley, L.J., Moch, J.M., van Donkelaar, A., Shen, L., Martin, R.V., 2018. Synoptic meteorological modes of variability for fine particulate matter ($PM_{2.5}$) air quality in major metropolitan regions of China. Atmos. Chem. Phys. 18 (9), 6733–6748. https://doi.org/10.5194/acp-18-6733-2018.
Liao, T., Gui, K., Jiang, W., Wang, S., Wang, B., Zeng, Z., Che, H., Wang, Y., Sun, Y., 2018. Air stagnation and its impact on air quality during winter in Sichuan and Chongqing, southwestern China. Sci. Total Environ. 635, 576–585. https://doi.org/10.1016/j.scitotenv.2018.04.122.
Ma, Q., Zhang, Q., Wang, Q., Yuan, X., Yuan, R., Luo, C., 2021. A comparative study of EOF and NMF analysis on downward trend of AOD over China from 2011 to 2019. Environ. Pollut. 288, 117713. https://doi.org/10.1016/j.envpol.2021.117713.
Malley, C.S., Michalopoulou, E., Kuylenstierna, J.C.I., 2023. Achieving Clean Air for Blue Skies in Seoul, Incheon and Gyeonggi. Republic of Korea, United Nations Environment Programme.
Oak, Y.J., Jacob, D.J., Pendergrass, D.C., Dang, R., Colombi, N.K., Chong, H., Lee, S., Kuk, S.K., Kim, J., 2025. Air quality trends and regimes in South Korea inferred from 2015–2023 surface and satellite observations. Atmos. Chem. Phys. 25 (5), 3233–3255. https://doi.org/10.5194/acp-25-3233-2025.
Park, H.-J., Ahn, J.-B., 2016. Combined effect of the Arctic Oscillation and the Western Pacific pattern on East Asia winter temperature. Clim. Dyn. 46 (9–10), 3205–3221. https://doi.org/10.1007/s00382-015-2750-5.
Pei, L., Yan, Z., Sun, Z., Miao, S., Yao, Y., 2018. Increasing persistent haze in Beijing: potential impacts of weakening East Asian winter monsoons associated with northwestern Pacific Sea surface temperature trends. Atmos. Chem. Phys. 18, 3173–3183. https://doi.org/10.5194/acp-18-3173-2018.
Peng, G., Wang, X., Wu, Z., Wang, Z., Yang, L., Zhong, L., Chen, D., 2011. Characteristics of particulate matter pollution in the Pearl River Delta region, China: an observational-based analysis of two monitoring sites. J. Environ. Monit. 13 (7), 1927–1934. https://doi.org/10.1039/c0em00776e.
Shaheen, A., Wu, R., Aldabash, M., 2020. Long-term AOD trend assessment over the Eastern Mediterranean region: a comparative study including a new merged aerosol product. Atmos. Environ. 238, 117738. https://doi.org/10.1016/j.atmosenv.2020.117736.
Shin, J., Shin, D., Müller, D., Noh, Y., 2023. Long-term analysis of AOD separated by aerosol type in East Asia. Atmos. Environ. 310, 119957. https://doi.org/10.1016/j.atmosenv.2023.119957.
Takaya, K., Nakamura, H., 2013. Interannual variability of the East Asian winter monsoon and related modulations of the planetary waves. J. Clim. 26, 9445–9461. https://doi.org/10.1175/JCLI-D-12-00842.1.
Tian, X., Gao, Z., 2019. Validation and accuracy assessment of MODIS C6.1 aerosol products over the heavy aerosol loading area. Atmosphere 10 (9), 548. https://doi.org/10.3390/atmos10090548.
Tian, X., Tang, C., Wu, X., Yang, J., Zhao, F., Liu, D., 2023a. The global spatial-temporal distribution and EOF analysis of AOD based on MODIS data during 2003–2021. Atmos. Environ. 302, 119722. https://doi.org/10.1016/j.atmosenv.2023.119722.
Tian, X., Tang, C., Wu, X., Yang, J., Zhao, F., Liu, D., 2023b. The global spatial-temporal distribution and EOF analysis of AOD based on MODIS data during 2003–2021. Atmos. Environ. 302, 119722. https://doi.org/10.1016/j.atmosenv.2023.119722.
Wang, J., Liu, Y., Ding, Y., 2020. Interdecadal relationship between the wintertime haze frequency over Beijing and mega-ENSO. Atmos. Sci. Lett. 21 (12), e1007. https://doi.org/10.1002/asl.1007.
Wang, X., Yi, W., Lv, Z., Deng, F., Zheng, S., Xu, H., Zhao, J., Liu, H., He, K., 2021. Ship emissions around China under gradually promoted control policies from 2016 to 2019. Atmos. Chem. Phys. 21 (18), 13835–13851. https://doi.org/10.5194/acp-21-13835-2021.
Wei, J., Li, Z., Peng, Y., Sun, L., 2019. MODIS Collection 6.1 aerosol optical depth products over land and ocean: Validation and comparison. Atmos. Environ. 201, 428–440. https://doi.org/10.1016/j.atmosenv.2018.12.004.
Xu, Z., Peng, Z., Zhang, N., Liu, H., Lei, L., Kou, X., 2024. Impact of meteorological conditions and reductions in anthropogenic emissions on PM2.5 concentrations in China from 2016 to 2020. Atmos. Environ. 318, 120265. https://doi.org/10.1016/j.atmosenv.2023.120265.
Yang, S., Lau, K.-M., Kim, K.-M., 2002. Variations of the East Asian jet stream and Asian-Pacific-American winter climate anomalies. J. Clim. 15 (3), 306–325. https://doi.org/10.1175/1520-0442(2002)015%3c0306:voteaj%3e2.0.co;2.
Yin, Z., Wang, H., Chen, H., 2017. Understanding severe winter haze events in the North China Plain in 2014: Roles of climate anomalies. Atmos. Chem. Phys. 17, 1641–1651. https://doi.org/10.5194/acp-17-1641-2017.
Yin, Z., Wang, H., Ma, X., 2019. Possible relationship between the Chukchi Sea ice in the early winter and the February haze pollution in the North China Plain. J. Clim. 32, 5179–5190. https://doi.org/10.1175/JCLI-D-18-0634.1.
Zhang, H., Wang, S., Hao, J., Wang, S., Chai, F., Li, M., 2016. Air pollution and control action in Beijing. J. Clean. Prod. 112, 1519–1527. https://doi.org/10.1016/j.jclepro.2015.04.092.
Zhang, Q., Ma, Q., Zhao, B., Liu, X., Wang, Y., Jia, B., Zhang, X., 2018a. Winter haze over North China Plain from 2009 to 2016: influence of emission and meteorology. Environ. Pollut. 242 (Part B), 1308–1318. https://doi.org/10.1016/j.envpol.2018.08.019.
Zhang, X., Zhong, J., Wang, J., Wang, Y., Liu, Y., 2018b. The interdecadal worsening of weather conditions affecting aerosol pollution in the Beijing area in relation to climate warming. Atmos. Chem. Phys. 18 (8), 5991–5999. https://doi.org/10.5194/acp-18-5991-2018.
Zhang, Q., Zheng, Y., Tong, D., et al., 2019. Drivers of improved PM2.5 air quality in China from 2013 to 2017. Proc. Natl. Acad. Sci. USA 116 (49), 24463–24469. https://doi.org/10.1073/pnas.1907956116.
Zhang, Y., Yin, Z., Zhou, B., Wang, H., 2022a. Possible relationship between January "Warm Arctic–Cold Eurasia" and February haze in North China. J. Clim. 35 (13), 4115–4130. https://doi.org/10.1175/JCLI-D-21-0465.1.
Zhang, S., Zeng, G., Wang, T., Yang, X., Iyakaremye, V., 2022b. Interannual relationship between displacement and intensity of East Asian jet stream and haze over eastern China in winter. Sci. Total Environ. 829. https://doi.org/10.1016/j.scitotenv.2022.154672.
Zhao, S., Li, J., Sun, C., 2016. Decadal variability in the occurrence of wintertime haze in central eastern China tied to the Pacific Decadal Oscillation. Sci. Rep. 6 (1), 27424. https://doi.org/10.1038/srep27424.
Zhao, S., Feng, T., Tie, X., Long, X., Li, G., Cao, J., Zhou, W., An, Z., 2018. Impact of climate change on Siberian High and wintertime air pollution in China in past two decades. Earth's Future 6 (2), 118–133. https://doi.org/10.1002/2017EF000682.
Zhao, W., Chen, S., Zhang, H., Wang, J., Chen, W., Wu, R., Xing, W., Wang, Z., Hu, P., Piao, J., Ma, T., 2022. Distinct Impacts of ENSO on Haze Pollution in the Beijing–Tianjin–Hebei Region between early and late Winters. J. Clim. 35 (2), 687–704. https://doi.org/10.1175/JCLI-D-21-0459.1.
Zheng, B., Tong, D., Li, M., Liu, F., Hong, C., Geng, G., Li, H., Li, X., Peng, L., Qi, J., Yan, L., Zhang, Y., Zhao, H., Zheng, Y., He, K., Zhang, Q., 2018. Trends in China's anthropogenic emissions since 2010 as the consequence of clean air actions. Atmos. Chem. Phys. 18, 14095–14111. https://doi.org/10.5194/acp-18-14095-2018.
Zou, Y., Wang, Y., Zhang, Y., Koo, J.-H., 2017. Arctic Sea ice, Eurasia snow, and extreme winter haze in China. Sci. Adv. 3 (3), e1602751. https://doi.org/10.1126/sciadv.1602751.